Received: 5 July 2019 | Revised: 4 November 2019 | Accepted: 29 November 2019

DOI: 10.1002/mrm.28139

FULL PAPER

Magnetic Resonance in Medicine

Assessment and correction of macroscopic field variations in 2D spoiled gradient-echo sequences

Martin Soellradl[1] | **Andreas Lesch**[2] | **Johannes Strasser**[1] | **Lukas Pirpamer**[1] | **Rudolf Stollberger**[2] | **Stefan Ropele**[1] | **Christian Langkammer**[1]

[1]Department of Neurology, Medical University of Graz, Graz, Austria

[2]Institute of Medical Engineering, Graz University of Technology, Graz, Austria

Correspondence
Martin Soellradl, Department of Neurology, Medical University of Graz, Auenbruggerplatz 22, Graz 8036, Austria.
Email: martin.soellradl@medunigraz.at

Funding information
Austrian Science Fund, Grant/Award Number: KLI 523 and P 30134

Purpose: To model and correct the dephasing effects in the gradient-echo signal for arbitrary RF excitation pulses with large flip angles in the presence of macroscopic field variations.

Methods: The dephasing of the spoiled 2D gradient-echo signal was modeled using a numerical solution of the Bloch equations to calculate the magnitude and phase of the transverse magnetization across the slice profile. Additionally, regional variations of the transmit RF field and slice profile scaling due to macroscopic field gradients were included. Simulations, phantom, and in vivo measurements at 3 T were conducted for R_2^* and myelin water fraction (MWF) mapping.

Results: The influence of macroscopic field gradients on R_2^* and myelin water fraction estimation can be substantially reduced by applying the proposed model. Moreover, it was shown that the dephasing over time for flip angles of 60° or greater also depends on the polarity of the slice-selection gradient because of phase variation along the slice profile.

Conclusion: Substantial improvements in R_2^* accuracy and myelin water fraction mapping coverage can be achieved using the proposed model if higher flip angles are required. In this context, we demonstrated that the phase along the slice profile and the polarity of the slice-selection gradient are essential for proper modeling of the gradient-echo signal in the presence of macroscopic field variations.

KEYWORDS

field inhomogeneities, myelin water fraction, R_2^*, relaxometry, slice profile, T_2^*

1 | INTRODUCTION

The sensitivity of gradient-echo (GRE) imaging to variations in magnetic susceptibility has led to a widespread range of applications in MRI. Approaches focusing on the signal decay are methods such as FMRI, in which the susceptibility difference between deoxyhemoglobin and oxyhemoglobin is measured,[1,2] perfusion MRI with gadolinium-based contrast agent,[3] R_2^* mapping by acquiring multi-gradient-echo (mGRE), or the determination of the myelin water fraction

(MWF) from analyzing the multi-exponential decay of GRE signal.[4] Methods exploiting the phase evolution of the signal are SWI[5] or QSM.[6] Quantitative susceptibility mapping and R_2^* contrast in the brain have been used to study iron content in inflammatory and neurodegenerative diseases.[7-11]

A challenge with quantifying mGRE data are the macroscopic field variations that arise, for example, from air/tissue boundaries, which lead to a faster signal decay and consequently mask tissue-relevant mesoscopic-scale and microstructure-scale R_2^* effects.[12] Approaches for correcting the influence of macroscopic field variations can be grouped into methods based on sequence design or postprocessing of conventional mGRE data. Methods requiring sequence adaptations aim to compensate intravoxel dephasing by varying the slice-rephasing gradient and/or by applying compensation gradients in the slice-selective direction.[13-17] Beyond sequence programming, a powerful approach is to simply increase spatial resolution,[18] which is not always feasible in a clinical setup with scan-time constraints or limited SNR.

The focus of the present work is the correction of the influence of macroscopic field variations by postprocessing of mGRE data. Given that for 2D-GRE acquisitions the slice thickness is usually much larger than the in-plane resolution, signal dephasing is largely driven by macroscopic field variations along the slice-selective direction z.[13] Assuming an ideal slice profile and a constant field gradient G_z as an approximation of the macroscopic field variation along z, the signal over time is sinc-weighted proportional to G_z and slice thickness.[12] Based on this theory, Fernandez-Seara and Wehrli[19] estimated G_z and R_2^* iteratively from the measured signal decay, which later was refined by initialization of G_z using the field map[20] and further extended by Yang et al by modeling field variation as a quadratic function, a condition that has become more relevant at ultrahigh-field MRI.[21] Depending on the RF excitation pulse, deviations from the ideal slice profile cause different dephasing in the presence of G_z. To account for various pulse shapes, Preibisch et al proposed a solution in which the signal modulation due to G_z and the slice profile is described by the envelope of the RF pulse.[22] This model allows to describe the signal decay for flip angles α of less than 60° and a much longer TR than the longitudinal relaxation time T_1 to avoid saturation of the slice profile.[22] To achieve a smooth signal decay, they have used exponential RF pulses[23] and compared them with sinc-shaped and sinc-Gauss shaped pulses for R_2^* mapping.[24]

Similar to R_2^* mapping, in MWF mapping, macroscopic field variations need to be accounted for.[25] Here, modeling approaches also assume an ideal slice profile.[25,26] In recent work, Lee et al combined z-shimming with modeling of the magnitude of the slice profile to achieve a better modeling of the signal decay.[27]

In contrast to the analytical solution in Preibisch et al,[22] which is limited by the small flip angle approximation,[28] we here propose a numerical model for solving the signal dephasing in the presence of G_z for an arbitrary excitation pulse and flip angle. Consequently, the model allows to benefit from increased SNR in measurements with interleaved slice acquisition, especially for large flip angles ($\alpha > 60°$). Extending the model from Hernando et al,[29] we also investigate variations of the transmit RF field B_1^+ and the effect of scaling of the slice profile due to superposition of G_z and the slice-selection gradient G_{slice}. We further demonstrate with phantom and in vivo measurements that, depending on the pulse shape for larger flip angles, the polarity of G_{slice} has to be considered, because through-slice phase variations can severely affect signal dephasing. With the proposed model, it is possible to substantially improve the quality of R_2^* maps and MWF maps acquired with arbitrary excitation pulses and flip angles.

2 | METHODS

2.1 | Theory

In the presence of macroscopic field variations $\Delta\omega(z)$, the signal $S(t)$ of a 2D spoiled GRE is proportional to the integral over the complex transverse magnetization $\underline{M}_{xy}(z) = \left|M_{xy}(z)\right| e^{i\varphi_{xy}(z)}$ weighted with $\Delta\omega(z)$ along the slice-selective direction z. Thus, depending on $\underline{M}_{xy}(z)$ and $\Delta\omega(z)$, additional signal dephasing is observed in contrast to theoretical mono-exponential signal decay with R_2^*. If $\Delta\omega(z)$ is smooth and slowly varying in space, $\Delta\omega(z)$ can be approximated with a linear function $\Delta\omega = \Delta\omega_0 + \gamma G_z z$ in each slice.[12] By assuming the origin of z being in the center of the slice, the equation for $S(t)$ reads as follows:

$$\begin{aligned} S(t) &= e^{-R_2^* t} \int_{-\infty}^{\infty} \underline{M}_{xy}\left(z, \alpha\xi, \lambda, E_1\right) e^{i\Delta\omega(z)t} dz \\ &\approx e^{-R_2^* t} \int_{-\infty}^{\infty} \underline{M}_{xy}\left(z, \alpha\xi, \lambda, E_1\right) e^{i\Delta\omega_0 t} e^{i\gamma G_z z t} dz \end{aligned} \tag{1}$$

where G_z denotes the field gradient and $\Delta\omega_0$ denotes the field offset. The value of $\underline{M}_{xy}(z)$ depends on several factors (including ξ, λ, and E_1), discussed in detail subsequently. Depending on the ratio of the TR and the T_1, which is included in the exponential term $E_1 = e^{-TR/T_1}$, and the effective flip angle $\alpha_{eff}(z)$ along the slice, the solution for $|M_{xy}(z)|$ changes according to the steady-state equation for spoiled GRE sequences[30] as follows:

$$\begin{aligned} &\left|M_{xy}\left(z, \alpha\xi, \lambda, E_1\right)\right| \\ &= S_0 \sin\left(\alpha_{eff}\left(z, \alpha\xi, \lambda\right)\right) \frac{1 - E_1}{1 - \cos\left(\alpha_{eff}\left(z, \alpha\xi, \lambda\right)\right) E_1}. \end{aligned} \tag{2}$$

When TR is much larger than T_1, Equation 2 simplifies and $|M_{xy}(z)|$ is obtained by the sine of α_{eff} times the equilibrium magnetization S_0:

$$\left|M_{xy}\left(z, \alpha\xi, \lambda, E_1 = 0\right)\right| = S_0 \sin\left(\alpha_{eff}\left(z, \alpha\xi, \lambda\right)\right). \quad (3)$$

Here, $\alpha_{eff}(z)$ is obtained for a certain slice-selection gradient G_{slice} and the applied excitation pulse with a certain shape and amplitude. For small flip angles, the slice profile $\alpha_{eff}(z)$ can be estimated for an RF pulse envelope $B_1(t)$ with the small flip angle approximation.[28] However, larger flip angles require solving the Bloch equations for $|M_{xy}(z)|$ and $\varphi_{xy}(z)$.

Extending previous studies, the factors ξ and λ were added to describe 2 effects that affect $\alpha_{eff}(z)$ and therefore signal dephasing. First, variations of the active transmit field (B_1^+) cause a deviation from the nominal flip angle α, which can change the effective flip angle profile $\alpha_{eff}(z)$, and therefore requires α to be scaled with ξ, obtained from the normalized B_1 map. Second, G_z is superimposed with G_{slice}, leading to either broadening or narrowing of the slice profile described by the factor λ[31] as follows:

$$\lambda = \frac{G_{slice}}{G_{slice} + G_z}. \quad (4)$$

To investigate the effect of the described parameters on signal dephasing in the presence of G_z, 4 different models have been studied. Summarizing Equation 1 in a tissue-specific signal component $S_{\text{tissue}}(t)$ (e.g., $S_{\text{tissue}}(t) = S_0 e^{-R_2^* t}$) and a component $F_i(t)$ describing the signal dephasing due to $\Delta\omega(z)$, the model $S_i(t)$ can be written as $S_i(t) = S_{\text{tissue}}(t) F_i(t)$. The 4 models are defined as follows:

$$S_1(t) = S_{\text{tissue}}(t)\, F_1(t) = S_{\text{tissue}}(t) \quad (5)$$

$$\begin{aligned} S_2(t) &= S_{\text{tissue}}(t)\, F_2(t) \\ &= S_{\text{tissue}}(t) \int_{-\infty}^{\infty} \left|M_{xy}\left(z, \alpha, \lambda = 1, E_1 = 0\right)\right| e^{i\gamma G_z z t} dz \end{aligned} \quad (6)$$

$$\begin{aligned} S_3(t) &= S_{\text{tissue}}(t)\, F_3(t) \\ &= S_{tissue}(t) \int_{-\infty}^{\infty} \left|M_{xy}\left(z, \alpha, \lambda = 1, E_1 = 0\right)\right| e^{i\varphi_{xy}(z, \alpha, \lambda = 1, E_1 = 0)} e^{i\gamma G_z z t} dz \end{aligned} \quad (7)$$

$$\begin{aligned} S_4(t) &= S_{\text{tissue}}(t)\, F_4(t) \\ &= S_{\text{tissue}}(t) \int_{-\infty}^{\infty} \left|M_{xy}\left(z, \alpha\xi, \lambda, E_1 = 0\right)\right| e^{i\varphi_{xy}(z, \alpha\xi, \lambda, E_1 = 0)} e^{i\gamma G_z z t} dz \end{aligned} \quad (8)$$

The model $S_1(t)$ serves as an uncorrected reference without modeling $\underline{M}_{xy}(z)$ and $\Delta\omega(z)$. Then, for $S_2(t)$, only the magnitude along the slice $|M_{xy}(z)|$ was considered neglecting $\varphi_{xy}(z)$. In $S_3(t)$, $\varphi_{xy}(z)$ was included, and in $S_4(t)$ the model was extended by additionally incorporating B_1^+ and λ variations.

2.2 | Numerical implementation

Signal dephasing due to G_z was estimated numerically for F_2 to F_4 assuming $E_1 = 0$. In the first step, $\underline{M}_{xy}$ was estimated for a certain RF excitation pulse and G_{slice} with a freely available numerical Bloch solver using *MATLAB* (MathWorks, Natick, MA).[32] Simulations were carried out with temporal resolution of 2 μs and spatial resolution of 80 μm with 2501 spatial points. The normalized envelope $B_1(t)$ was scaled to achieve $\alpha_{eff}(z = 0) = \alpha\xi$ in the center of the slice. Rather than estimating $\underline{M}_{xy}$ for each voxel with ξ and λ, calculations were accelerated by estimating $\underline{M}_{xy}$ in steps of $\Delta\xi = 0.05$ followed by linear interpolation to $\Delta\xi_{\text{intp}} = 0.005$. Variations of λ were incorporated by multiplying the sampling points along z with λ, to scale the thickness of the slice. In the last step, the integral along z for given G_z was solved by numerical integration. The source code can be found at: https://github.com/neuroimaging-mug.

2.3 | Simulations

To investigate the influence of the G_{slice} polarity and flip angle α on F_3, simulations for $\alpha = 30°$ and $\alpha = 90°$ with negative and positive polarity of G_{slice} were performed. Based on the vendor's standard GRE pulse, a sinc-Hanning-windowed excitation pulse with a pulse duration T_{pulse} of 2 ms and a bandwidth time (BWT) product of 2.7 was chosen for the experiments. A G_{slice} of 8.29 mT/m was determined with the Bloch solver to achieve a slice thickness Δz of 4 mm, as defined by the FWHM of $|M_{xy}|$ for $\alpha = 30°$. Based on the observed field gradients in phantom measurements, G_z was set to 100 μT/m for all simulations. In in vivo measurements of the brain, field gradients up to 300 μT/m have been reported in areas such as orbitofrontal cortex or inferior temporal lobe.[33]

Exploiting the relevance of individual parameters for modeling F_4, a sensitivity analysis was performed for φ_{xy}, B_1^+, and λ with the same sinc-Hanning-windowed excitation pulse. To estimate the relevance of φ_{xy}, simulations with $G_z = 100$ μT/m were carried out for F_4 with varying α from 10° to 90°, each with positive and negative G_{slice} polarity. Results were compared with simulations for model F_2 considering only the magnitude $|M_{xy}|$ of the slice profile ($\varphi_{xy} = 0$). For evaluation, the RMS error (RMSE) over time for each α between F_4 and F_2 was calculated.

The sensitivity for B_1^+ was simulated by scaling B_1^+ for each flip angle ($\alpha = 30°$ and $\alpha = 90°$) with a factor ξ (ranging from 0.6 to 1.4) for $G_z = 100$ μT/m. The results for F_4 obtained for different ξ were compared with those for $\xi = 1$ by plotting the RMSE. Same steps as for B_1^+ were carried out for λ by changing the value from 0.8 to 1.2.

A crucial assumption with the proposed models is that for a given α, TR is long enough to avoid changes of $|M_{xy}|$ due to incomplete T_1 relaxation $\left(E_1 = e^{-TR/T_1} \neq 0\right)$. Hence, the

steady-state solution in Equation 2 was included to estimate signal dephasing F_{T1} in the presence of $G_z = 100$ μT/m for different E_1:

$$F_{T1}(t) = \int_{-\infty}^{\infty} |M_{xy}(z, \alpha\xi, \lambda, E_1)| e^{i\varphi_{xy}(z, \alpha\xi, \lambda, E_1)} e^{i\gamma G_z z t} dz. \quad (9)$$

For each TR/T_1 (ranging from 1 to 5), the Ernst-angle α_{Ernst} was calculated and simulations with the sinc-Hanning-windowed RF pulse (T_{pulse} = 2 ms and BWT = 2.7) were carried out by setting $\alpha = \alpha_{Ernst}$, $\alpha = 0.8\ \alpha_{Ernst}$, and $\alpha = 0.6\ \alpha_{Ernst}$. Obtained results were compared by calculating the RMSE over time between F_{T1} and F_3.

2.4 | Phantom experiments

To validate the results from the simulations of dephasing effects for different α and G_{slice}, polarity phantom measurements were performed. For the phantom, a plastic cylinder (Ø = 12 cm and length = 20 cm) was filled with agarose gel (5 g/L), which was doped with 110 μmol/L MAGNEVIST to shorten the T_1.

The phantom was scanned on a 3 T MRI system (Magnetom Prisma; Siemens, Erlangen, Germany) twice by a mGRE sequence with $\alpha = 30°$ and $\alpha = 90°$, each with alternating polarity of G_{slice}. The same sinc-Hanning-windowed excitation pulse (T_{pulse} = 2 ms and BWT = 2.7) as for the simulations was used, and $|G_{slice}| = 8.29$ mT/m was used to achieve $\Delta z = 4$ mm for $\alpha = 30°$.

Other sequence parameters were as follows: FOV = 128 × 128 mm^2, in-plane resolution = 1 × 1 mm^2, 32 monopolar echoes with bandwidth = 500 Hz/px, TE_1 = 4 ms, ΔTE = 5 ms, TR = 3 seconds, 25 slices, with 0% interslice gap. For B_1 mapping, a Bloch-Siegert sequence with the same resolution was used.[34]

The G_z map was obtained by using the central difference from the field map ΔB_0 to estimate the gradient in the ith slice:

$$G_z(x, y, z_i) = 0.5 \frac{\Delta B_0(x, y, z_{i+1}) - \Delta B_0(x, y, z_{i-1})}{\Delta z}. \quad (10)$$

Single side difference was used for the first ($i = 1$) and last slice ($i = N$). The value of ΔB_0 was estimated from a linear fit of the first 6 echoes of the unwrapped phase (PRELUDE unwrapping[35]). From the measured data, R_2^* maps were estimated in *MATLAB* using the lsqnonlin() function with models S_1 to S_4.

As indicated in Supporting Information Figure S1, when varying G_{slice} amplitude slightly within the model, it was found that results could be further improved when using $G_{slice} = 8.5$ mT/m for all analyses.

2.5 | Influence of TR/T_1

Phantom measurements with different TRs (125 ms, 250 ms, 500 ms, 1 second, 1.5 seconds, 2 seconds, 3 seconds, and 5 seconds) and α (30°, 60°, and 90°) were carried out with the mGRE sequence to investigate steady-state effects for modeling. A Bloch-Siegert sequence was used for B_1 mapping.[34] In addition, T_1 was estimated with an inversion recovery sequence with 6 TIs (100 ms, 200 ms, 400 ms, 800 ms, 1.6 seconds, and 3.6 seconds), and the excited slice was measured with 0.5 × 0.5 mm^2 in-plane resolution by changing the readout direction to the slice direction. Results were evaluated by estimating R_2^* with model S_4 for each TR and α.

2.6 | In vivo R_2^* and MWF experiments

To evaluate the proposed modeling for in vivo application, R_2^* and MWF mapping experiments were performed on the same 3 T MRI system with 10 subjects (age range = 26-50 years). The study was approved by the local ethics committee, and all subjects gave written informed consent. In addition, subjects were scanned with an anatomical MPRAGE with 1-mm^3 isotropic resolution for regional evaluation of R_2^* and MWF maps.

For R_2^* mapping, subjects were scanned twice with a mGRE sequence with alternating G_{slice} polarity using a sinc-Hanning-windowed excitation pulse (T_{pulse} = 2 ms and BWT = 2.7) with $\alpha = 85°$ (Ernst angle assuming T_1 = 1 second). Other sequence parameters were as follows: FOV = 256 × 208 mm^2, in-plane resolution = 1 × 1 mm^2, $|G_{slice}|$ = 11.05 mT/m to achieve Δz = 3 mm, 17 monopolar echoes with bandwidth = 500 Hz/px, TE_1 = 2.87 ms, ΔTE = 3.59 ms, TR = 2.5 seconds, and 30 slices with 0% interslice gap. The last echo was a navigator echo at TE_{navi} = 65.4 ms, to correct for physiologically induced field variations.[36] Then for each channel, the nth phase-encoding line $S_n(k_x, TE)$ was corrected as described by Wen et al[37]:

$$S_n^c(k_x, TE) = S_n(k_x, TE) \exp\left(-i \frac{\phi_n - \phi_1}{TE_{navi}} TE\right), \quad (11)$$

where ϕ_n and ϕ_1 are the mean phase values of the nth navigator echo and the reference phase of the first navigator echo, respectively. To account for phase accumulation after excitation, the estimated phase difference was scaled with the TE. Afterward, corrected k-space data were combined with the method proposed in Luo et al.[38]

For B_1 mapping, a highly accelerated method based on the Bloch-Siegert shift was used.[39] The field map for calculating G_z was obtained from the difference of the unwrapped phase of the first and third echo divided by TE difference. From

the data, R_2^* maps were obtained using the models S_1, S_3, and S_4. The difference between the models was assessed regionally by calculating the mean and SD of R_2^* in all subjects in gray matter and global white-matter masks. Gray matter masks were segmented from the MPRAGE images with FSL FIRST,[40] and the global white matter masks with SIENAX,[41] part of FSL.[42] All masks were affinely registered to mGRE space with FSL FLIRT.[43,44]

For MWF mapping, all subjects were scanned with a slightly adapted mGRE sequence to account for the fast decaying myelin water component. Short echo spacing ($\Delta TE = 2.2$ ms) was achieved with a bipolar readout gradient, which was inverted in a second acquisition to compensate for phase errors between even and odd echoes. Other sequence parameters were as follows: sinc-Hanning-windowed excitation pulse with $T_{pulse} = 1$ ms and BWT = 2, $\alpha = 85°$, $G_{slice} = 14.15$ mT/m, FOV = 255×105 mm^2, in-plane resolution = 1.14×1.14 mm^2, $\Delta z = 4$ mm, 27 bipolar echoes with bandwidth = 500 Hz/Px, $TE_1 = 2.37$ ms, $\Delta TE = 2.2$ ms, TR = 2 seconds, $TE_{navi} = 63.8$ ms, 25 interleaved slices with 0% interslice gap, and total scan time = 12 minutes. Again, a highly accelerated B_1 map was acquired.[39]

After correction of the data with the navigator echoes, the 2 mGRE images were registered using FSL FLIRT[45] before averaging. The MWF estimation was based on a multi-exponential T_2^* relaxation times model[46] with M = 200 water components:

$$S_{\text{tissue}}(TE) = \sum_{j=1}^{M} s_j \exp\left(-\frac{TE}{T_{2,j}^*}\right). \quad (12)$$

Evaluation of data was performed by estimating MWF maps using models S_1, S_3, and S_4 with the nonnegative least squares algorithm of the MERA toolbox[47] and a cutoff for myelin water $T_{2my}^* < 25$ ms.[48] For S_3 and S_4, the measured signal S was corrected with F_3 and F_4, respectively, before parameter estimation.

Regional evaluation of MWF maps was performed in white matter tracts with the JHU white-matter atlas.[49] The atlas was nonlinearly registered with FSL FNIRT to the MPRAGE images and transformed to the mGRE space using FSL FLIRT.[43,44] Before evaluation, masks were manually checked and adjusted with ITK-SNAP.[50]

In a single scan session, 8 mGRE data sets were acquired from 1 subject (male, age = 29) using 4 different excitation pulses with $\alpha = 30°$ and 85° for each pulse. The first pulse was a 2-ms-long Gaussian pulse with $\sigma = 280$ µs ($B_1(t) = e^{-\frac{t}{2\sigma}}$), and the other 3 were sinc-Hanning-windowed pulses with different BWT = 2, 2.7, and 8 and $T_{pulse} = 1$ ms, 2 ms, and 4 ms. The value of $G_{slice} = 10.56$ mT/m, 18.87 mT/m, 11.05 mT/m, and 15.65 mT/m was estimated with the Bloch solver for $\Delta z = 3$ mm and $\alpha = 30°$. Other sequence parameters, as well as B_1 mapping, were as described for in vivo R_2^* mapping. The differences between the pulses were assessed by estimating R_2^* maps with S_4.

3 | RESULTS

3.1 | Simulations

Figure 1 shows the simulation results for sinc-Hanning-windowed excitation pulse with positive and negative G_{slice} polarity for $\alpha = 30°$ and $\alpha = 90°$. It reveals that the polarity has no influence on $|M_{xy}(z)|$ of the slice profile (Figure 1A,B), whereas $\varphi_{xy}(z)$ is inverted when flipping polarity (Figure 1C,D). Consequently, F_3 depends on the polarity of G_{slice} (Figure 1E,F), an effect that is more strongly pronounced for $\alpha = 90°$.

The sensitivities of the model parameters $\varphi_{xy}(z)$, B_1^+, λ, and TR/T_1 are illustrated in Figure 2. When neglecting $\varphi_{xy}(z)$ in Figure 2A, the RMSE substantially increases for $\alpha > 40°$ with larger RMSE for negative G_{slice}. For $\alpha = 90°$, the RMSE is 5.5% for negative polarity and 4.5% for positive polarity, respectively.

The sensitivity for B_1^+ variations in Figure 2B depends strongly on the nominal flip angle α. For $\alpha = 30°$, the RMSE was below 0.5% for all simulated values of ξ ($\alpha_{effective} = \alpha * \xi$), with a moderate increase for $\alpha = 60°$ to 1% for ξ = 1.3. With 2.9%, the RMSE was 3 times higher for $\alpha = 90°$.

The influence of λ on the signal is relatively small compared with B_1^+ and $\varphi_{xy}(z)$ with an RMSE of 0.8% for a strong G_z with 500 µT/m and minimal dependency on α (Figure 2C).

The simulated error due to neglecting T_1 for different TR/T_1 in Figure 2D shows an exponential decrease of the RMSE with increasing TR/T_1 for all simulated flip angles. For all TR/T_1 ratios, the highest RMSE was estimated when using the Ernst-angle α_{Ernst} and declines nonlinearly for 0.8 α_{Ernst} and 0.6 α_{Ernst}. For example, for $TR/T_1 = 1$, the RMSE decreases from 2.8% to 1.8% to 1.2% for all simulated flip angles, whereas for $TR/T_1 = 2$ the RMSE reduces from 1.2% to 0.8% to 0.5%.

When comparing the simulated errors by neglecting φ_{xy} in Figure 2A with T_1 effects in Figure 2D, the RMSE of φ_{xy} becomes dominant with increasing TR/T_1 ratio. Given that $TR/T_1 > 2$, which results in $\alpha_{Ernst} > 82°$, the RMSE is smaller than 1.2%, whereas the RMSE due to neglecting φ_{xy} is at least higher than 3.3% depending on the G_{slice} polarity.

3.2 | Phantom experiments

The R_2^* values estimated with the mono-exponential model S_1 are plotted as a function of G_z for $\alpha = 30°$ and $\alpha = 90°$ with positive and negative G_{slice} polarity in Figure 3. The value of

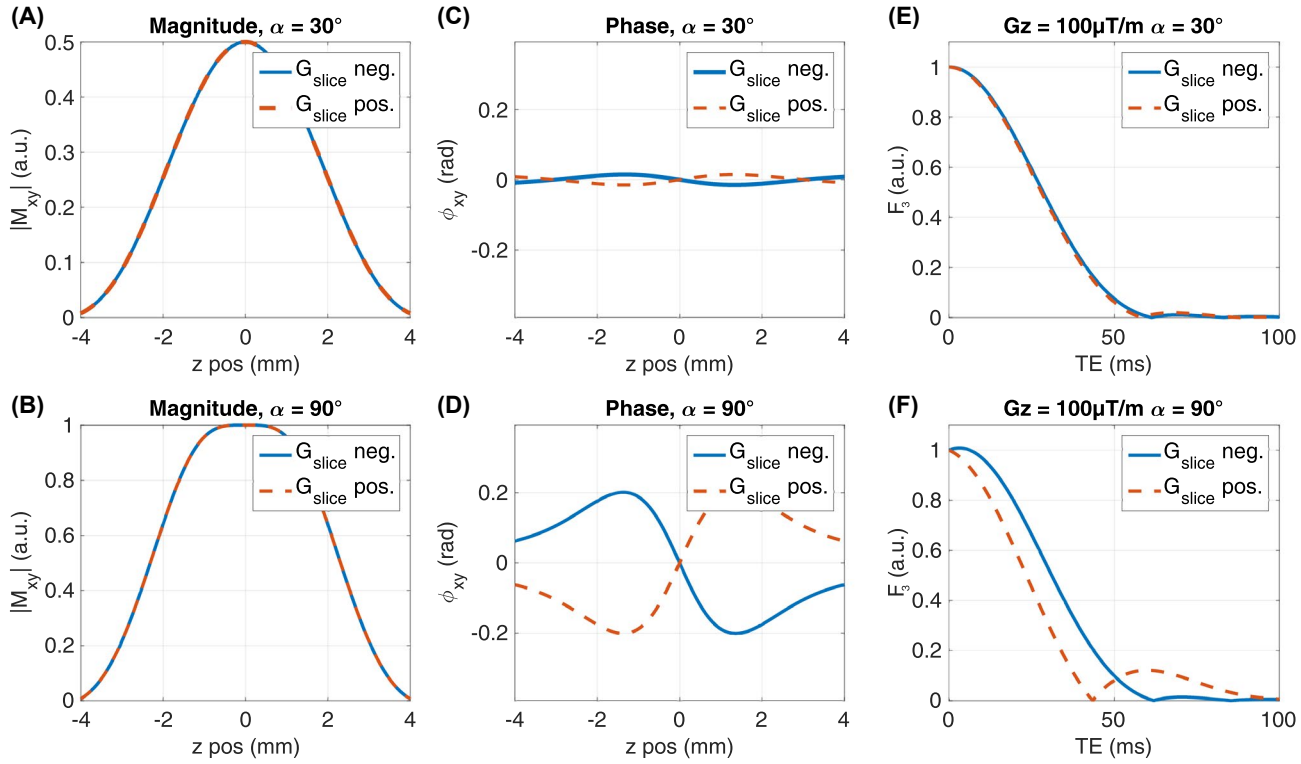

FIGURE 1 Simulation results for magnitude $|M_{xy}|$ (A,B) and phase φ_{xy} (C,D) of the slice profile and the resulting dephasing F_3 (E,F) with a macroscopic field gradient $G_z = 100$ µT/m for a sinc-Hanning-windowed excitation pulse (pulse duration $T_{pulse} = 2$ ms, bandwidth time product BWT = 2.7). For each α (top $\alpha = 30°$, bottom $\alpha = 90°$), simulations were performed with positive (red dotted line) and negative (solid blue line) G_{slice} polarity. There is no difference in the magnitude (A,B) but the mirrored phase for $\alpha = 90°$ (D) causes different F_3 (F)

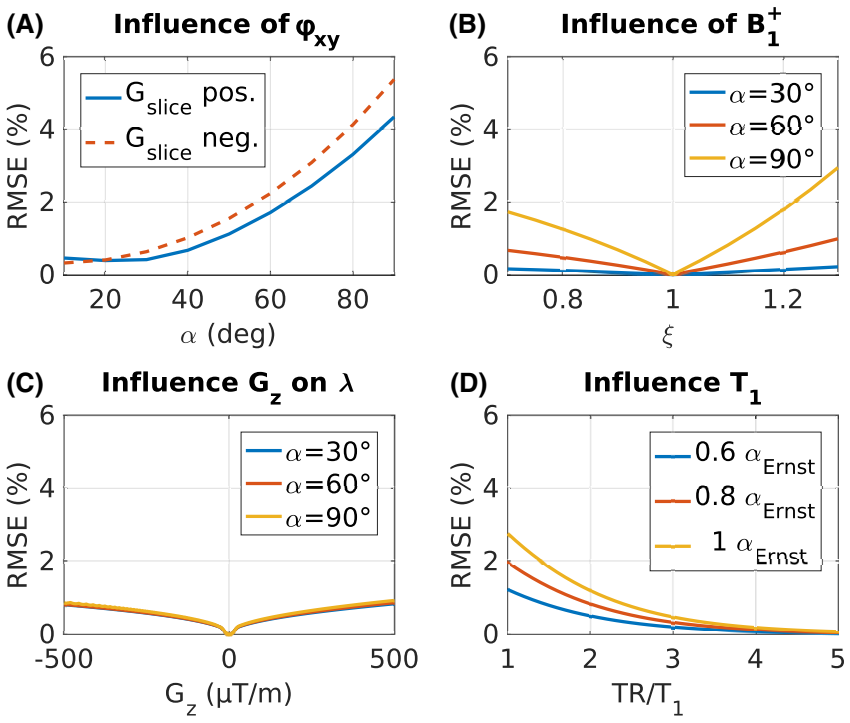

FIGURE 2 Sensitivity analysis of the numerical model parameters. A, Comparison of the effect of including phase φ_{xy} in F_4 versus a magnitude model F_2 for positive and negative G_{slice} polarity and $G_z = 100$ µT/m. B, Effects of B_1^+ variations in F_4 with a macroscopic field gradient $G_z = 100$ µT/m. C, Influence of G_z on the slice encoding described with λ. D, The RMS error (RMSE) for neglecting T_1 for different TR/T_1 ratios is plotted assuming $G_z = 100$ µT/m. For each TR/T_1, the RMSE was estimated between the F_4 and F_{T1} for α_{Ernst}, 0.8 α_{Ernst}, and 0.6 α_{Ernst}

R_2^* increases proportional to G_z for $\alpha = 30°$ (Figure 3A) with up to 8-times higher R_2^* values for $G_z = 150$ µT/m than for $G_z = 0$ µT/m. For $\alpha = 30°$, negligibly small differences between the polarity of G_{slice} and the sign of G_z were found, whereas for $\alpha = 90°$ (Figure 3B), positive and negative G_z yield different R_2^* values and a dependency on the polarity of G_{slice}. Moreover,

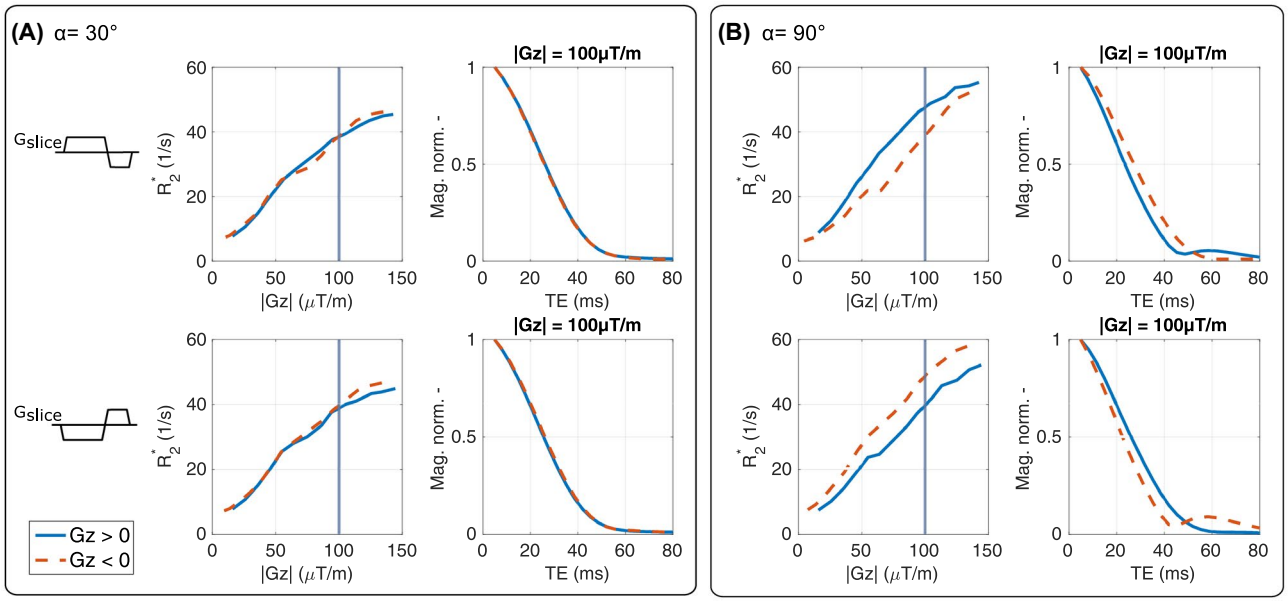

FIGURE 3 Comparison of R_2^* values estimated from the phantom experiments with the mono-exponential model S_1 are plotted as function of G_z for $\alpha = 30°$ (A) and $\alpha = 90°$ (B) with positive and negative slice-selection gradient G_{slice}. Additionally, the averaged normalized signal decay is plotted for $|G_z| = 100$ µT/m. The dotted red line represents a positive G_z and the solid blue line represents a negative G_z. For $\alpha = 30°$, no relevant differences between the polarity of G_{slice} and G_z are observed, whereas for $\alpha = 90°$, flipped G_{slice} polarity substantially affects R_2^*

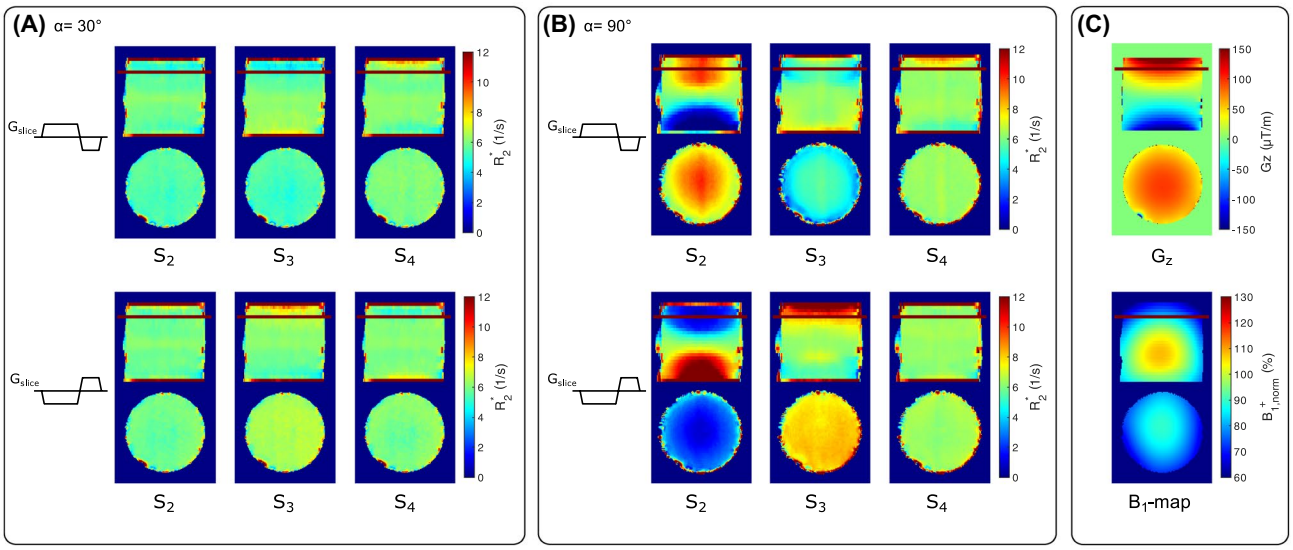

FIGURE 4 Coronal and axial slices of estimated R_2^* maps from the phantom measurements for different signal models (S_2 -S_4). Although all correction models yield relatively comparable R_2^* values for $\alpha = 30°$ (A), the high flip angle results for $\alpha = 90°$ (B) highlight the effect of B_1^+ and λ correction. Full modeling with S_4 also eliminates the influence of the polarity of the slice-selection gradient G_{slice} at $\alpha = 90°$. The corresponding G_z maps and B_1 maps are shown in (C)

Figure 3 shows the normalized averaged signal decay for $|G_z| = 100$ µT/m plotted with positive and negative G_z, explaining the difference in estimated R_2^* values. For $\alpha = 90°$ with positive G_{slice} and $G_z > 0$ (blue line), the signal decays faster than for $G_z < 0$ (red) and vice versa when switching G_{slice} polarity.

Figure 4 compares the R_2^* maps obtained from fits using models S_2, S_3, and S_4 for $\alpha = 30°$ (Figure 4A) and $\alpha = 90°$ (Figure 4B), each with positive and negative G_{slice} polarity. In addition, the G_z map and B_1 map are illustrated in Figure 4C. Although results for $\alpha = 30°$ are comparable for all models, considerable differences for $\alpha = 90°$ between models and G_{slice} polarity were found. When using only the magnitude $|M_{xy}|$ in model S_2 to estimate R_2^* for $\alpha = 90°$, it was not possible to recover R_2^* without the influence of G_z. The R_2^* values for $G_z > 0$ were overestimated for positive G_{slice} and underestimated for $G_z < 0$, and switching to negative G_{slice} polarity inverted the

results. Extending the model S_2 by adding φ_{xy} in S_3 yields better maps, which are influenced less by the G_{slice} polarity. Additionally, including B_1^+ and λ in S_4 substantially improves R_2^* maps, with minimal differences between G_{slice} polarities. Further, estimated R_2^* maps using S_4 with $\alpha = 90°$ are comparable with maps estimated from $\alpha = 30°$ for both G_{slice} polarities.

Figure 5 illustrates the effects of neglecting T_1 for signal modeling. Estimated R_2^* maps with S_4 (Figure 5A) indicate an overestimation of R_2^*, depending on TR and α in the presence of G_z (Figure 5B). For $\alpha = 30°$, increased R_2^* values are observable only up to a TR of 500 ms, whereas for $\alpha = 90°$ these effects extend up to a TR of 1.5 seconds. These TR values correspond to a TR/T_1 ratio of 0.67 and 2.01 for the estimated $T_1 = 740$ ms. The origin for the R_2^* overestimation is shown in Figure 5C, where the averaged measured signal along the slice profile is plotted. Depending on α and TR, the steady-state solution changes, causing a modeling error in the presence of G_z. Between different TRs for $\alpha = 30°$, the profiles show less variations compared with $\alpha = 90°$, leading to different signal dephasing for the same G_z. In addition to T_1 effects, for TR > 2 seconds, SNR benefits can be observed for maps acquired with $\alpha = 90°$ compared with $\alpha = 30°$.

3.3 | In vivo experiments

In vivo results of R_2^* maps obtained with models S_1 and S_4 are illustrated in Figure 6 for both G_{slice} polarities. When comparing S_1 (Figure 6A,B) with S_4 (Figure 6D,E), much higher R_2^* values are observed in maps using S_1 compared with S_4, thereby minimizing the effects of G_z. In addition, the difference map between positive and negative G_{slice} polarity for each model reveals strong variations of R_2^* values with up to 10 s^{-1} for S_1 in areas with strong G_z (Figure 6C). In contrast, maps estimated with S_4 substantially suppressed the effect of G_{slice} polarity with difference values below 1 s^{-1} (Figure 6F).

In Table 1 the regional evaluation of R_2^* values with the corresponding mean $|G_z|$ across all subjects is presented. Compared with the other models, the highest R_2^* values were obtained with S_1 in all anatomical regions. In addition, the difference between G_{slice} polarities increases with the mean $|G_z|$ value in each region for S_1. For example, in the caudate nucleus, where the smallest $|G_z|$ was observed with 20 μT/m, the difference between polarities is below 0.1 s^{-1}, whereas in the brainstem it is 7.46 s^{-1} at a mean $|G_z|$ of 89 μT/m. The R_2^* values generally decrease when using S_2, but the difference between polarities slightly increases compared with S_1. Applying models S_3 and S_4 reduces the discrepancy between G_{slice} polarities to a maximum of 2.01 s^{-1} and 1.25 s^{-1} in the brainstem. In all other regions the difference is much smaller, with values below 0.8 s^{-1}. Between models S_3 and S_4, rather small changes can be observed generally.

The difference between R_2^* estimation with S_4 and S_3 is shown in Figure 7, pointing out the effect of modeling B_1^+

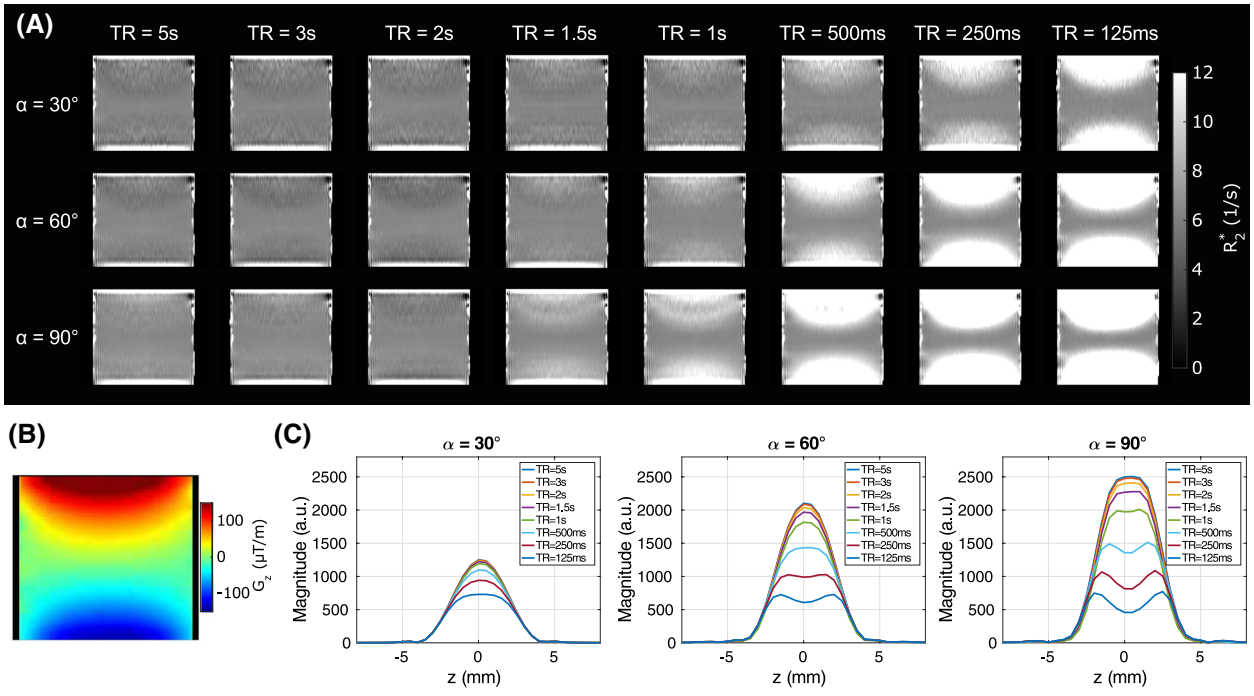

FIGURE 5 Experimental evaluation of TR/T_1 dependency for R_2^* modeling in phantom measurements. A, Coronal R_2^* maps were estimated using S_4 for different TR and α. The minimum TR required for avoiding T_1 effects increases with the magnitude of G_z (B) and α. The value of $T_1 = 740 \pm 86$ ms was estimated with an inversion-recovery sequence. C, The measured signal along the slice for each α and TR shows the different steady-state solutions

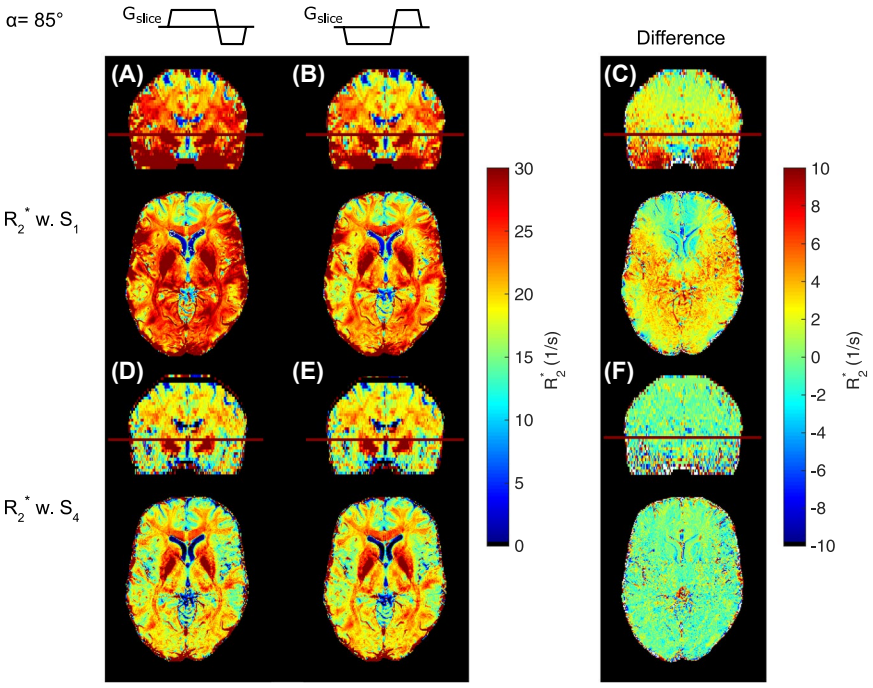

FIGURE 6 Comparison of coronal and axial R_2^* maps obtained from mono-exponential model S_1 (A,B) with maps from the proposed numerical model S_4 (D,E) for positive and negative slice-selection gradient G_{slice}. C,F, Difference map between G_{slice} polarities for each model. The S_1 model shows R_2^* overestimation and substantial impact of the G_{slice} polarity (C), which were mitigated using S_4 (F)

TABLE 1 R_2^* values (s^{-1}) from models S_1 to S_4 in different brain regions for 10 subjects with the corresponding $|G_z|$ values for positive and negative G_{slice}

Region	G_{slice}	S_1	S_2	S_3	S_4	$\lvert G_z \rvert$ (μT/m)
Global WM	pos.	26.34 (1.16)	21.11 (0.61)	20.10 (0.58)	19.63 (0.62)	43.06 (8.81)
	neg.	23.72 (0.97)	18.17 (0.58)	19.89 (0.54)	20.17 (0.50)	43.68 (8.40)
Caudate Nucleus	pos.	23.36 (1.53)	21.46 (1.47)	21.81 (1.40)	21.82 (1.40)	20.47 (3.57)
	neg.	23.41 (1.61)	21.58 (1.32)	21.58 (1.28)	21.52 (1.27)	20.42 (3.22)
Pallidum	pos.	39.83 (2.78)	36.56 (2.58)	35.60 (2.65)	34.85 (2.71)	34.38 (8.75)
	neg.	36.86 (2.75)	33.50 (3.08)	35.07 (2.85)	35.61 (2.81)	34.03 (8.73)
Putamen	pos.	29.11 (2.14)	25.78 (1.70)	25.02 (1.76)	24.49 (1.80)	32.69 (5.84)
	neg.	26.97 (2.06)	23.52 (2.05)	24.91 (1.90)	25.28 (1.87)	32.90 (5.87)
Thalamus	pos.	25.84 (1.80)	22.34 (0.64)	21.33 (0.62)	20.34 (0.84)	33.65 (8.75)
	neg.	22.61 (0.97)	18.80 (1.24)	20.50 (0.87)	21.22 (0.74)	34.41 (8.83)
Brainstem	pos.	35.15 (7.97)	20.34 (2.07)	17.58 (1.77)	15.10 (1.60)	88.61 (35.73)
	neg.	27.70 (6.99)	11.21 (1.96)	15.08 (1.53)	16.45 (1.55)	89.90 (34.79)

Note: The R_2^* and $|G_z|$ values are shown as mean (SD).

Abbreviations: neg., negative; pos., positive; and WM, white matter.

and λ in S_4. When visually comparing the difference maps in Figure 7A,B, a strong correspondence between the magnitude of G_z (Figure 7C) and B_1^+ (Figure 7D) can be observed for both G_{slice} polarities.

The R_2^* maps from data acquired with 4 different excitation pulses and 2 different flip angles are shown in Figure 8. Visually, only minor differences among all maps are observable. Higher SNR can be observed in maps with $\alpha = 85°$ compared with $\alpha = 30°$. Mean regional R_2^* values are in good agreement after applying models S_3 and S_4 (Supporting Information Table S1). For example, in global white matter, the largest SD of R_2^* between the acquisitions was found for S_1 with 1.59 s^{-1}, due to the different pulses and flip angles. By using S_2, it decreases to 0.82 s^{-1}, and for S_3 and S_4 the estimated values are 0.19 s^{-1} and 0.2 s^{-1}, respectively.

Figure 9 shows representative slices of MWF maps from 5 subjects obtained with models S_1, S_3, and S_4. It shows that with S_1, in areas with strong G_z, such as in the frontal and temporal lobe, the MWF estimation was not feasible, whereas the proposed approaches allowed a reconstruction in these areas. Between maps with models S_3 and S_4, no considerable

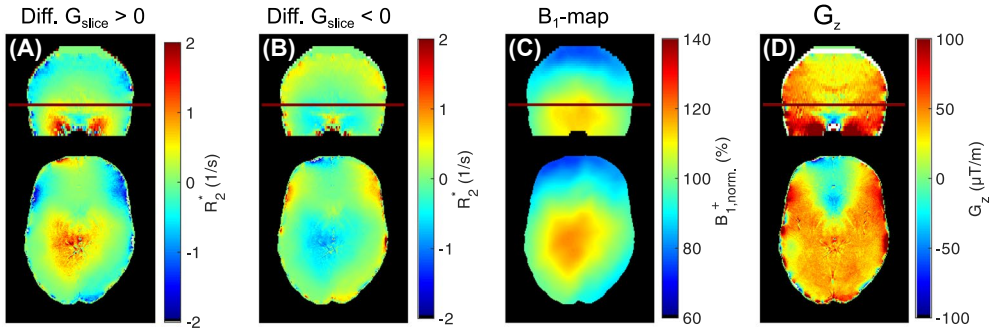

FIGURE 7 Difference between R_2^* maps estimated with S_4 (includes B_1^+ and λ variations) and S_3 for positive (A) and negative slice-selection gradient G_{slice} (B). Coronal (upper row) and axial (lower row) views are shown. C, B_1 map. D, G_z map. Depending on G_{slice} polarity, R_2^* varies in areas with higher B_1^+ and G_z variations

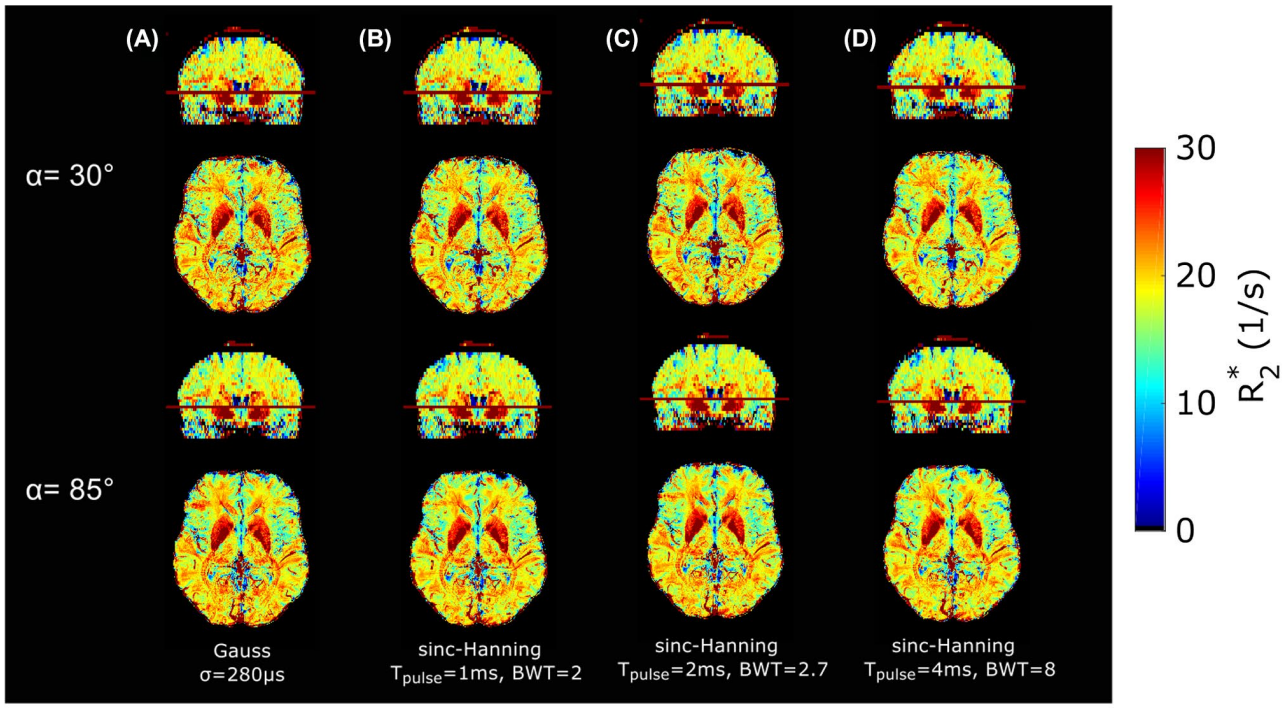

FIGURE 8 R_2^* maps estimated with model S_4 from multi-gradient-echo (mGRE) data acquired with 4 different excitation pulses (A-D) for $\alpha = 30°$ (top row) and $\alpha = 85°$ (bottom row). Regional evaluation of R_2^* can be found in Supporting Information Table S1

differences were found, indicating that B_1^+ and λ have a neglectable small influence.

As shown in Figure 9, the MWF in the genu of the corpus callosum is underestimated with S_1 because of G_z. Using S_3 and S_4 enabled us to recover MWF values in these areas with a median of 12.09% and 12.66%, respectively. Our MWF results are within the range of reported values: For the genu of the corpus callosum, Lee et al[27] reported approximately 12% for their postprocessing approach, and Alonso-Ortiz et al[26] reported approximately 16%. Furthermore, in the body of the corpus callosum, the proposed models yield to an increase of MWF from 3.7% with S_1 to 6.65% and 6.67% for S_3 and S_4, respectively. Interestingly, this analysis demonstrated that rather small $|G_z|$ with around 10 μT/m in the body of the corpus callosum severely affects MWF estimation when using the simple model S_1. Supporting Information Table S2 summarizes the median MWF values in all 10 subjects in different white-matter regions for models S_1, S_3, and S_4.

4 | DISCUSSION

In this work we have introduced a numerical model for the signal dephasing of 2D mGRE sequences for arbitrary excitation pulses in the presence of a macroscopic field gradient G_z. In contrast to existing analytical solutions, our model is based on solving the Bloch equations numerically, which allows to

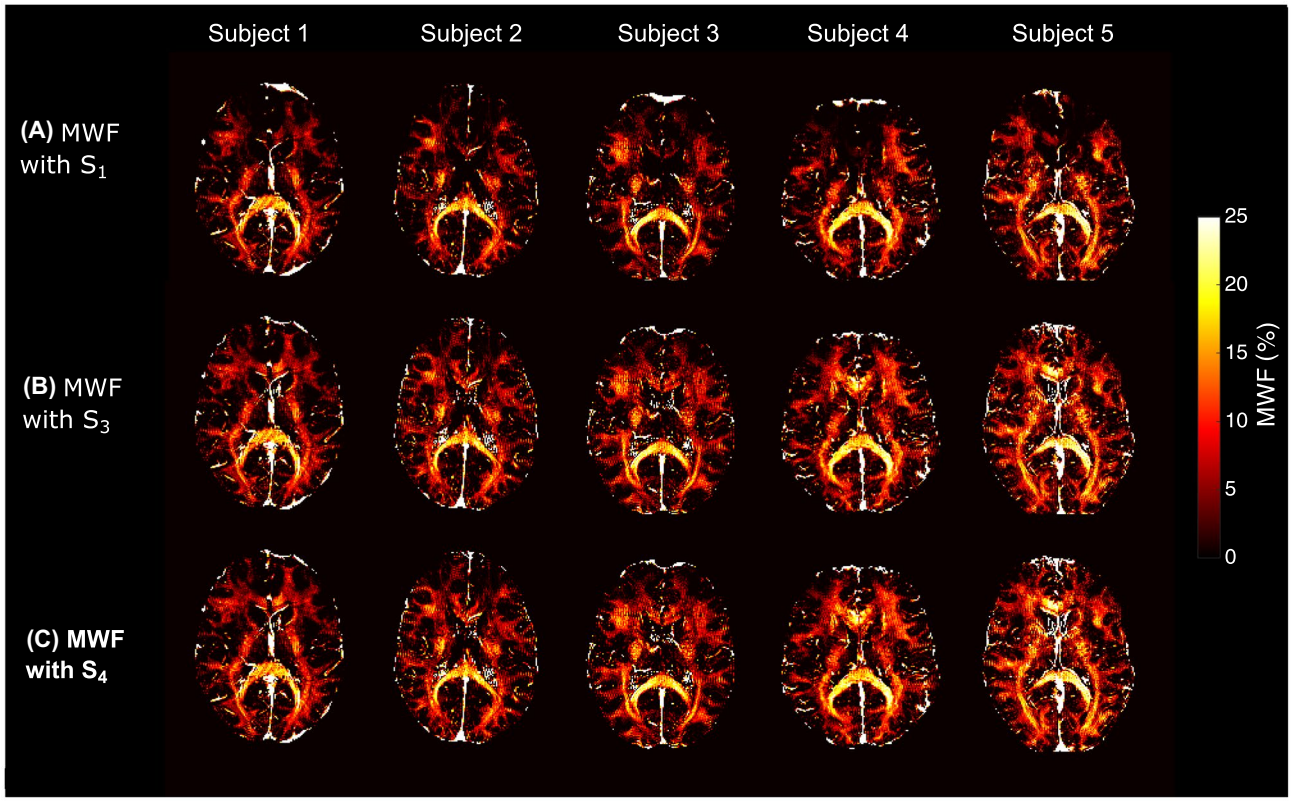

FIGURE 9 Representative myelin water fraction (MWF) maps from 5 subjects, obtained using models S_1 (A), S_3 (B), and S_4 (C). The proposed models S_3 and S_4 allow us to recover MWF values in areas strongly affected by the field gradient G_z (e.g., in frontal areas)

estimate signal dephasing for any given flip angle α. We have shown that it is indispensable to consider the phase along the slice profile φ_{xy} and the polarity of the slice-selection gradient G_{slice} for describing the signal dephasing for higher α. In our experiments, the threshold was approximately 60°, but this may also vary with the RF-pulse shape.

Compared with existing models,[19,20,22-24,26,27] which include the slice profile and assume linear varying macroscopic field variations, with the proposed model it is possible to explain different signal decays for different signs of G_z observed when using larger flip angles. As illustrated in Figure 1, this mismatch is explained by the phase variation φ_{xy} along the slice profile, causing either a faster dephasing or a short period of rephasing followed by dephasing. Consequently, depending on the pulse shape and effective flip angle, the polarity of the gradient G_{slice} must be included for modeling, as switching polarity inverts φ_{xy} and thus signal dephasing.

In addition to the polarity dependency of G_{slice}, the effects of B_1^+ variations and scaling of the slice profile with λ have been investigated in model S_4. However, changes in R_2^* due to B_1^+ and λ were relatively small compared with S_3 (Table 1). Evaluation has been performed under the assumption that with an ideal model the estimated R_2^* maps should be independent of G_{slice} polarity. For the models S_1 and S_2, strong differences between G_{slice} polarities were found, primarily due to φ_{xy}, and by using S_3 it was substantially reduced, which indicates improved modeling. However, the main challenge for validation of the models was that, in vivo, no ground truth was available.

Another important aspect is the assumption that TR for a given α is sufficiently long to avoid T_1 influence in the presence of G_z. The experimental results in Figure 5A are in accordance with the simulation results in Figure 2D, where the error decreases with TR/T_1, and the minimum TR/T_1 required enlarges with α. To gain SNR, it is desirable to use α_{Ernst}, but care should be taken to prevent potential errors due to T_1 and B_1^+. By increasing TR/T_1, both the α_{Ernst} and the overall SNR increase; however, the errors due to B_1^+ are magnified. For example, as illustrated in Figure 2, when $TR/T_1 = 2$, the error when neglecting T_1 is about 1.2% for $\alpha = \alpha_{Ernst} = 77°$. By comparing errors caused by B_1^+ variation, a deviation of $\xi = 1.15$ leads to errors in a similar range. Thus, without knowing T_1, it is not possible to separate these effects, but it can be adjusted by the RF pulse shape. For instance, to estimate R_2^* more accurately, longer RF pulses can be used to obtain a slice profile closer to the ideal, rectangular shape. This would have the advantage that signal dephasing is influenced less by B_1^+ and TR/T_1, but it would lead to stronger φ_{xy} variations and zero crossings due to the sinc-shaped signal decay in the presence of G_z. However, for MWF estimation, very short

pulses are needed, which will be more sensitive to these factors. Optimization of the RF pulses for specific applications was beyond of the scope of this work, but different pulses and their effects can be included and studied with the provided framework.

When comparing different modeling approaches, we can distinguish between models that fit parameters of F(t) from the signal decay[19,21] and models that use information from the pulse and field map to calculate F(t).[22-24] Approaches that fit F(t) are more flexible in terms of model deviations from the ideal slice profile. For example, the sinc function used in the model approach by Fernandez-Seara and Wehrli[19] is well-suited to model a variety of signal decays observed with different excitation pulses. Similarly, when modeling the macroscopic field as a quadratic function, the effects of a nonideal slice profile are inherently compensated for.[21] However, in these models, the parameter estimation is often challenging due to the multiplication of F(t) with $S_{\text{tissue}}(t)$, thereby requiring the acquisition of many echoes. In contrast, with the analytical solution or our proposed numerical approach for F(t), only the parameters of the tissue model S_{tissue} need to be estimated. Thus, if the properties of the RF pulse are available, a detailed description of F(t) is possible, favoring a closed or numerical solution. To select an appropriate model for a certain RF pulse and flip angle, the provided framework can be used to evaluate the expected error of different modeling approaches. If φ_{xy} might be neglected for a specific RF pulse and flip angle, then an analytic solution yields a faster solution of F(t).

This work has similar limitations as other related postprocessing approaches.[19,20,22,24,26,29] The assumption of a linear varying magnetic field in slice direction might not hold in some areas with large susceptibility changes, which is especially pronounced at higher field strengths. However, as we have solved the dephasing along the slice direction by numerical integration, the model can also easily be adapted to describe the dephasing also for a quadratic varying magnetic field. Furthermore, in-plane dephasing effects are neglected. In 2D acquisitions the slice thickness is usually much larger than the in-plane resolution, but this might reduce accuracy in areas where the macroscopic in-plane field variations are high. A possible solution to account for in-plane dephasing could be to calculate the voxel spread function in-plane as proposed by Yablonskiy et al[51] and multiply the result with F_3 or F_4, respectively. Given that G_z is rather strong and that the signal dephasing is driven primarily by G_z, a reliable parameter estimation is difficult to achieve due to the fast signal decay. To overcome this issue, for MWF and R_2^* it has been shown that z-shim gradients between echoes can improve maps by rephasing the signal with appropriated compensation gradients.[27,52] Therefore, future work will focus on extending our model by including the moment of the z-shim gradients in the modeling to describe the signal dephasing accordingly for every echo.

In addition to variations of the macroscopic field, variation of the phase offset φ_0 at TE = 0 could potentially influence signal dephasing. Contributions to φ_0 in phased array coils can be divided into receive coil–dependent (receive sensitivity B_1^-) and receive coil–independent (e.g., B_1^+ phase).[53] To reconstruct the navigator-corrected raw data, a multi-echo approach was used to combine the individual coil data.[38] In this approach, for each coil, images from all echoes are multiplied with the complex conjugate of the first echo, which removes inherently all components of φ_0 of the coil combined data. The development of the proposed models pointed out that the use of navigator echoes is highly recommended to compensate for phase errors arising from physiological fluctuations. As illustrated in Supporting Information Figure S2, depending on the subject's reconstruction of parameter maps, not having the navigator echoes caused similar artifacts, as reported by Nam et al.[54] If variations of φ_0 should be included, a ROEMER/SENSE reconstruction could be applied, as an example.[55,56]

The scan time of the proposed applications is about 6 minutes for R_2^* maps and 12 minutes for MWF maps. This is clinically acceptable for whole-brain investigations, but further investigations will also focus on combination with accelerated imaging methods such as 2D CAIPIRINHA.[57]

5 | CONCLUSIONS

Proper modeling of the signal dephasing in the presence of G_z for larger flip angles requires the consideration of $|M_{xy}|$ and φ_{xy} with correct G_{slice} polarity. Furthermore, B_1^+ and λ variations can potentially lead to a bias in the estimated model parameters, depending on the excitation pulse. Consequently, the proposed model allows to minimize the effects of G_z, which is highly relevant for accurate R_2^* and MWF mapping of the entire brain based on 2D mGRE.

ORCID

Martin Soellradl https://orcid.org/0000-0002-3760-5578
Andreas Lesch https://orcid.org/0000-0003-2492-3566
Johannes Strasser https://orcid.org/0000-0002-2396-5126
Christian Langkammer https://orcid.org/0000-0002-7097-9707

REFERENCES

1. Kwong KK, Belliveau JW, Chesler DA, et al. Dynamic magnetic resonance imaging of human brain activity during primary sensory stimulation. *Proc Natl Acad Sci*. 1992;89:5675–5679.
2. Ogawa S, Menon RS, Tank DW, et al. Functional brain mapping by blood oxygenation level-dependent contrast magnetic resonance

imaging. A comparison of signal characteristics with a biophysical model. *Biophys J*. 1993;64:803–812.
3. Villringer A, Rosen BR, Belliveau JW, et al. Dynamic imaging with lanthanide chelates in normal brain: contrast due to magnetic susceptibility effects. *Magn Reson Med*. 1988;6:164–174.
4. Du YP, Chu R, Hwang D, et al. Fast multislice mapping of the myelin water fraction using multicompartment analysis of T2* decay at 3T: a preliminary postmortem study. *Magn Reson Med*. 2007;58:865–870.
5. Haacke EM, Xu Y, Cheng Y-CN, Reichenbach JR. Susceptibility weighted imaging (SWI). *Magn Reson Med*. 2004;52:612–618.
6. Li L, Leigh JS. Quantifying arbitrary magnetic susceptibility distributions with MR. *Magn Reson Med*. 2004;51:1077–1082.
7. Bagnato F, Hametner S, Yao B, et al. Tracking iron in multiple sclerosis: a combined imaging and histopathological study at 7 Tesla. *Brain*. 2011;134:3602–3615.
8. Pitt D, Boster A, Pei W, et al. Imaging cortical lesions in multiple sclerosis with ultra–high-field magnetic resonance imaging. *Arch Neurol*. 2010;67:812–818.
9. Fukunaga M, Li T-Q, van Gelderen P, et al. Layer-specific variation of iron content in cerebral cortex as a source of MRI contrast. *Proc Natl Acad Sci*. 2010;107:3834–3839.
10. Brass SD, Chen NK, Mulkern RV, Bakshi R. Magnetic resonance imaging of iron deposition in neurological disorders. *Top Magn Reson Imaging*. 2006;17:31–40.
11. Bartzokis G, Tishler TA. MRI evaluation of basal ganglia ferritin iron and neurotoxicity in Alzheimer's and Huntingon's disease. *Cell Mol Biol (Noisy-le-grand)*. 2000;46:821–833.
12. Yablonskiy DA. Quantitation of intrinsic magnetic susceptibility-related effects in a tissue matrix. *Phantom study. Magn Reson Med*. 1998;39:417–428.
13. Frahm J, Merboldt K-D, Hänicke W. Direct FLASH MR imaging of magnetic field inhomogeneities by gradient compensation. *Magn Reson Med*. 1988;6:474–480.
14. Yang QX, Williams GD, Demure RJ, Dardzinski BJ, Mosher TJ, Smith MB. Removal of local field gradient artifacts in GE images by slice excitation profile imaging (GESEPI) in high field. *Magn Reson Med*. 1998;39:402–409.
15. Truong TK, Chakeres DW, Scharre DW, Beversdorf DQ, Schmalbrock P. Blipped multi gradient-echo slice excitation profile imaging (bmGESEPI) for fast T2* measurements with macroscopic B0 inhomogeneity compensation. *Magn Reson Med*. 2006;55:1390–1395.
16. Constable RT. Functional MR imaging using gradient-echo echo-planar imaging in the presence of large static field inhomogeneities. *J Magn Reson Imaging*. 1995;5:746–752.
17. Wild JM, Wayne Martin WR, Allen PS. Multiple gradient echo sequence optimized for rapid, single-scan mapping of R2* at high B0. *Magn Reson Med*. 2002;48:867–876.
18. Young IR, Cox IJ, Bryant DJ, Bydder GM. The benefits of increasing spatial resolution as a means of reducing artifacts due to field inhomogeneities. *Magn Reson Imaging*. 1988;6:585–590.
19. Fernández-Seara MA, Wehrli FW. Postprocessing technique to correct for background gradients in image-based R*2 measurements. *Magn Reson Med*. 2000;44:358–366.
20. Dahnke H, Schaeffter T. Limits of detection of SPIO at 3.0 T using T2* relaxometry. *Magn Reson Med*. 2005;53:1202–1206.
21. Yang X, Sammet S, Schmalbrock P, Knopp MV. Postprocessing correction for distortions in T2* decay caused by quadratic cross-slice B0 inhomogeneity. *Magn Reson Med*. 2010;63:1258–1268.
22. Preibisch C, Volz S, Anti S, Deichmann R. Exponential excitation pulses for improved water content mapping in the presence of background gradients. *Magn Reson Med*. 2008;60:908–916.
23. Baudrexel S, Volz S, Preibisch C, et al. Rapid single-scan T2*-mapping using exponential excitation pulses and image-based correction for linear background gradients. *Magn Reson Med*. 2009;62:263–268.
24. Hirsch NM, Preibisch C. T2* mapping with background gradient correction using different excitation pulse shapes. *AJNR. Am J Neuroradiol*. 2013;34:E65–E68.
25. Hwang D, Kim D-H, Du YP. In vivo multi-slice mapping of myelin water content using T2* decay. *NeuroImage*. 2010;52:198–204.
26. Alonso-Ortiz E, Levesque IR, Paquin R, Pike GB. Field inhomogeneity correction for gradient echo myelin water fraction imaging. *Magn Reson Med*. 2017;78:49–57.
27. Lee D, Lee J, Lee J, Nam Y. Single-scan z-shim method for reducing susceptibility artifacts in gradient echo myelin water imaging. *Magn Reson Med*. 2018;80:1101–1109.
28. Hoult D. The solution of the bloch equations in the presence of a varying B1 field—an approach to selective pulse analysis. *J Magn Reson*. 1979;35:69–86.
29. Hernando D, Vigen KK, Shimakawa A, Reeder SB. R2* mapping in the presence of macroscopic B0 field variations. *Magn Reson Med*. 2012;68:830–840.
30. Ernst RR, Anderson WA. Application of Fourier transform spectroscopy to magnetic resonance. *Rev Sci Instrum*. 1966;37:93–102.
31. Reichenbach JR, Venkatesan R, Yablonskiy DA, Thompson MR, Lai S, Haacke EM. Theory and application of static field inhomogeneity effects in gradient-echo imaging. *J Magn Reson Imaging*. 1997;7:266–279.
32. Aigner CS, Clason C, Rund A, Stollberger R. Efficient high-resolution RF pulse design applied to simultaneous multi-slice excitation. *J Magn Reson*. 2016;263:33–44.
33. Weiskopf N, Hutton C, Josephs O, Turner R, Deichmann R. Optimized EPI for fMRI studies of the orbitofrontal cortex: compensation of susceptibility-induced gradients in the readout direction. *Magn Reson Mater Phys Biol Med*. 2007;20:39–49.
34. Sacolick LI, Wiesinger F, Hancu I, Vogel MW. B1 mapping by Bloch-Siegert shift. *Magn Reson Med*. 2010;63:1315–1322.
35. Smith SM, Jenkinson M, Woolrich MW, et al. Advances in functional and structural MR image analysis and implementation as FSL. *NeuroImage*. 2004;23(Suppl 1):S208–S219.
36. Hu X, Kim SG. Reduction of signal fluctuation in functional MRI using navigator echoes. *Magn Reson Med*. 1994;31:495–503.
37. Wen J, Cross AH, Yablonskiy DA. On the role of physiological fluctuations in quantitative gradient echo MRI: implications for GEPCI, QSM, and SWI. *Magn Reson Med*. 2015;73:195–203.
38. Luo J, Jagadeesan BD, Cross AH, Yablonskiy DA. Gradient echo plural contrast imaging—signal model and derived contrasts: T2*, T1, Phase, SWI, T1f, FST2*, and T2*-SWI. *NeuroImage*. 2012;60:1073–1082.
39. Lesch A, Schlöegl M, Holler M, Bredies K, Stollberger R. Ultrafast 3D Bloch-Siegert B_1^+-mapping using variational modeling. *Magn Reson Med*. 2019;81:881–892.
40. Patenaude B, Smith SM, Kennedy DN, Jenkinson M. A Bayesian model of shape and appearance for subcortical brain segmentation. *NeuroImage*. 2011;56:907–922.
41. Smith SM, Zhang Y, Jenkinson M, et al. Accurate, robust, and automated longitudinal and cross-sectional brain change analysis. *NeuroImage*. 2002;17:479–489.

42. Smith SM, Jenkinson M, Woolrich MW, et al. Advances in functional and structural MR image analysis and implementation as FSL. *NeuroImage*. 2004;23:S208–S219.
43. Jenkinson M, Smith S. A global optimisation method for robust affine registration of brain images. *Med Image Anal*. 2001;5:143–156.
44. Jenkinson M, Bannister P, Brady M, Smith S. Improved optimization for the robust and accurate linear registration and motion correction of brain images. *NeuroImage*. 2002;17:825–841.
45. Jenkinson M, Bannister P, Brady M, Smith S. Improved optimization for the robust and accurate linear registration and motion correction of brain images. *NeuroImage*. 2002;17:825–841.
46. Whittall KP, MacKay AL. Quantitative interpretation of NMR relaxation data. *J Magn Reson*. 1989;84:134–152.
47. Does M.Multi Exponential Relaxation Analysis toolbox for MATLAB. https://github.com/markdoes/MERA. Accessed June 2, 2019.
48. Lenz C, Klarhöfer M, Scheffler K. Feasibility of in vivo myelin water imaging using 3D multigradient-echo pulse sequences. *Magn Reson Med*. 2012;68:523–528.
49. Mori S (Susumu), Crain BJ. *MRI Atlas of Human White Matter*. Amsterdam, Netherlands: Elsevier; 2005.
50. Yushkevich PA, Piven J, Hazlett HC, et al. User-guided 3D active contour segmentation of anatomical structures: significantly improved efficiency and reliability. *NeuroImage*. 2006;31:1116–1128.
51. Yablonskiy DA, Sukstanskii AL, Luo J, Wang X. Voxel spread function method for correction of magnetic field inhomogeneity effects in quantitative gradient-echo-based MRI. *Magn Reson Med*. 2013;70:1283–1292.
52. Han D, Nam Y, Gho SM, Kim DH. Volumetric R2* mapping using z-shim multi-echo gradient echo imaging. *Magn Reson Med*. 2015;73:1164–1170.
53. Robinson SD, Bredies K, Khabipova D, Dymerska B, Marques JP, Schweser F. An illustrated comparison of processing methods for MR phase imaging and QSM: combining array coil signals and phase unwrapping. *NMR Biomed*. 2017;30.
54. Nam Y, Kim D-H, Lee J. Physiological noise compensation in gradient-echo myelin water imaging. *NeuroImage*. 2015;120:345–349.
55. Pruessmann KP, Weiger M, Scheidegger MB, Boesiger P. SENSE: sensitivity encoding for fast MRI. *Magn Reson Med*. 1999;42:952–962.
56. Roemer PB, Edelstein WA, Hayes CE, Souza SP, Mueller OM. The NMR phased array. *Magn Reson Med*. 1990;16:192–225.
57. Breuer FA, Blaimer M, Mueller MF, et al. Controlled aliasing in volumetric parallel imaging (2D CAIPIRINHA). *Magn Reson Med*. 2006;55:549–556.

SUPPORTING INFORMATION

Additional supporting information may be found online in the Supporting Information section.

FIGURE S1 Coronal R_2^* maps from the phantom measurements ($\alpha = 90°$) estimated for a varying slice-selection gradient G_{slice} within the model. The most homogenous map was obtained with $G_{slice} = 8.5$ mT/m

FIGURE S2 A,B, The MWF maps from 2 subjects. Maps are shown without and with correction of the raw data with the phase of the navigator echo

TABLE S1 Influence of pulse shape and flip angle for modeling R_2^*. Note: The R_2^* values (s^{-1}) were estimated with models S_1 to S_4 from mGRE data acquired with 4 different pulses and $\alpha = 30°$ and $\alpha = 85°$. It shows a flip angle and pulse shape dependency for S_1 in all regions. By applying S_2, differences decrease but R_2^* values remain larger for $\alpha = 85°$ than for $\alpha = 30°$. With S_3 and S_4, the flip angle dependency can be improved, leading to minimal differences of R_2^* between the pulses. In the S_4 model, B_1^+ and λ have a small additional effect on R_2^* estimation, compared with S_3

TABLE S2 Myelin water fraction values (%) with models S_1, S_3, and S_4 in different white matter regions for 10 subjects. Note: The MWF values are shown as median (interquartile range). The corresponding $|G_z|$ values are listed as mean (SD)

How to cite this article: Soellradl M, Lesch A, Strasser J, et al. Assessment and correction of macroscopic field variations in 2D spoiled gradient-echo sequences. *Magn Reson Med*. 2020;84:620–633. https://doi.org/10.1002/mrm.28139